Distribution of Partial Melt Beneath Changbaishan/Paektu Volcano, China/Democratic People's Republic of Korea

James O. S. Hammond[1], Jian-Ping Wu[2], Kyong-Song Ri[3], Wei Wei[4], Jong-Nam Yu[3], and Clive Oppenheimer[5]

[1]Department of Earth and Planetary Sciences, Birkbeck, University of London, London, UK, [2]Institute of Geophysics, China Earthquake Administration, Beijing, China, [3]Earthquake Administration, Pyongyang, Democratic People's Republic of Korea, [4]Institute of Geology, China Earthquake Administration, Beijing, China, [5]Department of Geography, University of Cambridge, Cambridge, UK

Abstract   Changbaishan/Paektu volcano straddles the border between the Democratic People's Republic of Korea and China. It was responsible for one of the largest eruptions in history, the "Millennium Eruption' of 946 CE. An episode of unrest between 2002 and 2005, characterized by inflation and seismicity, refocused attention on this volcano. While satellite remote sensing has provided synoptic observations, ground-based surveillance has hitherto supported only disparate analyses and geophysical interpretations on either side of the border. Here, we derive receiver functions using seismic records from both Democratic People's Republic of Korea and China. H-κ stacking indicates thick crust (up to 40 km) and high average crustal V_P/V_S (up to 1.93) beneath the volcano. Grid search inversions constrain a significant velocity reduction at 4–8 km depth (below sea level), and harmonic analysis suggests this dips away from the volcano, with shallowest depths centered beneath the volcano. Common conversion point migrations show that this anomaly extends ∼30 km from the volcano summit and possibly as far as neighboring volcanoes. The colocation of the velocity reduction with a zone of high-conductivity, low-velocity, and low-density material at the depth of the inflation source implicated in the 2002–2005 unrest indicates that partial melt is present directly beneath Changbaishan/Paektu, likely recharged during the episode of unrest. Our study highlights the importance of continued surveillance of the volcano and the need for further geophysical studies to constrain more fully the triggers for unrest and controls on its evolution.

Plain Language Summary   Changbaishan/Mount Paektu volcano is the largest volcano in the China/Korean Peninsula and was responsible for one of the largest eruptions in history in 946 CE. In 2002–2005 volcanic unrest led to renewed interest in the volcano, yet to date the volcano's location on the China/Democratic People's Republic of Korea border has limited study of the whole volcanic system. In this unique collaboration, we use data from both China and Democratic People's Republic of Korea to image the crustal structure beneath the volcano. We show that the top of a magma reservoir is present at ˜6 km, extending up to 30 km from the volcano and this may have been recharged during the recent volcanic unrest.

1. Introduction

Changbaishan/Mount Paektu (CMP) is a large volcano situated on the border between the Democratic People's Republic of Korea (DPRK) and the People's Republic of China (China). It lies far from any tectonic plate boundary (Figure 1), but seismic tomography models show a deep portion of the Pacific slab lying horizontally in the transition zone beneath and to the east of the Korean Peninsula (Wei et al., 2012; Zhao, 2004). This has led to the formulation of the "big mantle wedge" model as the dominant theory for the origin of CMP, where a second stage of dewatering occurs in the transition zone and results in compositionally buoyant material rising, causing melting in the uppermost mantle (Zhao, 2004). However, other models suggest a hole in the Pacific slab may let subslab hot material rise (Tang et al., 2014) or invoke shallow processes such as lithospheric delamination (Wei et al., 2019) or edge-driven convection as the cause of volcanism in this region (Kim et al., 2017).
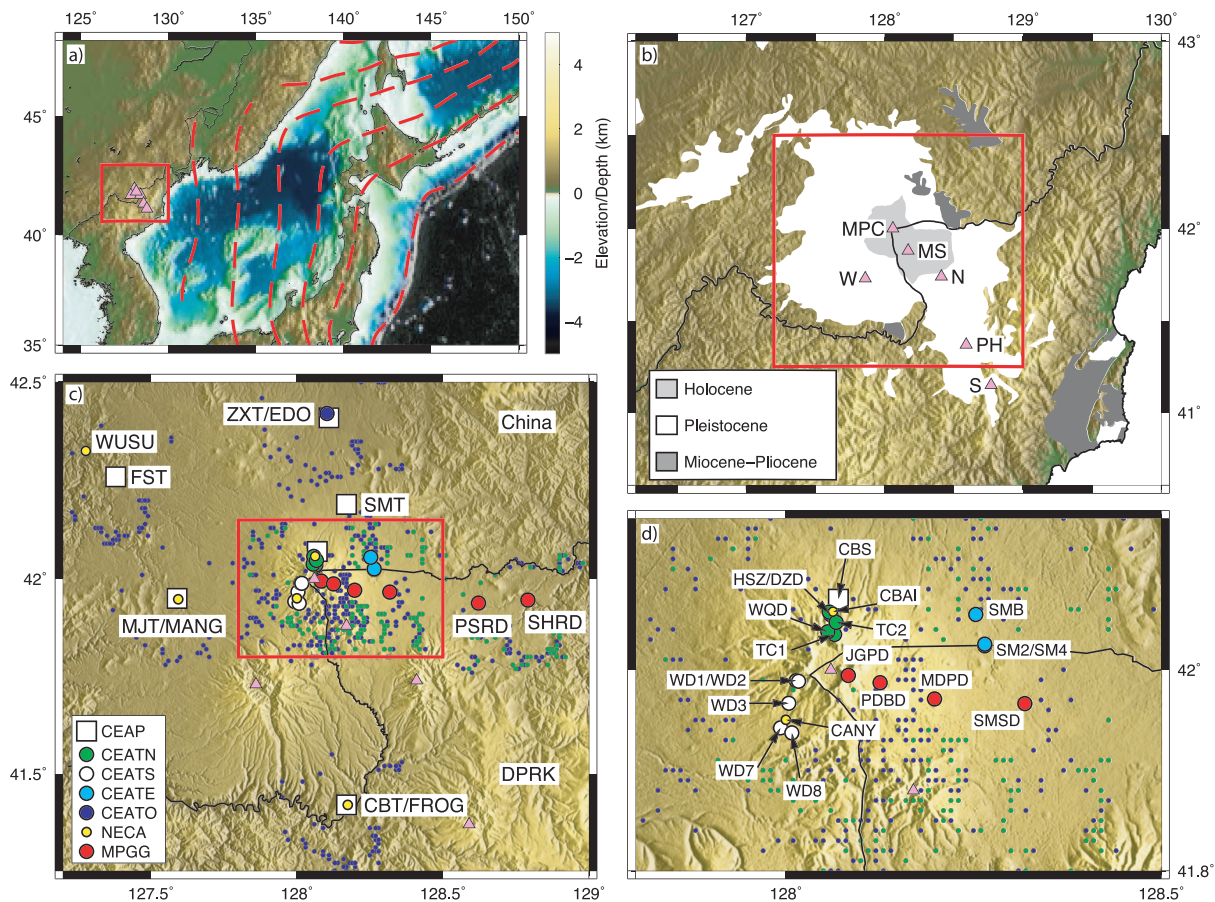
Figure 1. (a) Regional tectonic setting of CMP. Red dashed lines show the Pacific slab contours at 100 km intervals (Hayes et al., 2018). (b) Simplified map showing major magmatism around CMP. Major magmatic centers are shown as pink triangles; CMP = Changbaishan/Mount Paektu; WM = Wangtian'e/Mount Mangchona; GJ = Mount Ganbaek/Jianbaishan; PB = Mount South Potae/Baotaishan (after Paek, 1996; Ren et al., 2013). (c) Location of seismometers used in this study. CEAP = CEA permanent stations; CEATN, CEATS, CEATE, and CEATO = CEA temporary stations (north, south, and east groups and other stations, respectively); NECA = Northeast China array (Wu, 1998); MPGG = Mount Paektu Geoscientific Group array (The Mount Peaktu Geoscientific Group [MPGG] 2013). Small green and blue circles show the piercing points of the RF at 35 km depth in an ISAP91 velocity model for Kyong-Song et al. (2016) and this study showing the increase in coverage in this study. (d) Location of seismometers close to CMP.

The volcano is the site of one of the largest eruptions of the Common Era, the so-called Millennium Eruption of 946 CE (Oppenheimer et al., 2017; Xu et al., 2013), which ejected an estimated 24 ± 5 km^3 of dense rock equivalent of tephra. Ash fallout is recorded in Japan and the Kuril Islands (Horn & Schmincke, 2000; Nanayama et al., 2003) and Greenland (Sun et al., 2014). Petrological and geochemical studies suggest that a complex magmatic system existed prior to the Millennium Eruption with commenditic magma and traychitic magmas present at shallow depths (Horn & Schmincke, 2000; Pan et al., 2017; Ramos et al., 2016), with a deeper-sourced basaltic magma input triggering the 946 CE eruption (Pan et al., 2017). Debate exists about whether more recent eruptions have occurred (Pan et al., 2017; Ramos et al., 2016, 2019), but an episode of unrest between 2002 and 2005, characterized by increased seismicity, surface deformation, and volcanic gas emissions showed that the volcano continues to be active. This unrest was explained as the result of a shallow intrusion of basaltic magma (Wei et al., 2013; Xu et al., 2012). This episode did not culminate in eruption but renewed interest in the volcano (e.g., Stone, 2011).

Geophysical studies have probed the underlying structure of CMP, including the use of magnetotelluric methods (Qiu et al., 2014; Tang et al., 2001), along with a range of seismological techniques using controlled sources (Liu et al., 2005; Song et al., 2007; Zhang et al., 2002), attenuation (Wu et al., 2006), receiver functions (RFs) (Hetland et al., 2004; Kyong-Song et al., 2016; Wu et al., 2009; Zhu et al., 2019), and surface waves (Kim et al., 2017; Yang et al., 2019; Zhu et al., 2019). These studies have identified zones of low conductivity, high attenuation, or low seismic velocity, which in turn have been interpreted as indicators of partial melt

and/or high temperatures in the crust beneath CMP. However, a significant limitation to these studies has been their reliance on data and observations from either China (e.g., Hetland et al., 2004; Kim et al., 2017; Wu et al., 2006; Wu et al., 2009; Zhu et al., 2019; Zhang et al., 2002) or DPRK (Kyong-Song et al., 2016) but, until now, not from cross-border experiments or integrated data sets.

Some of the best constraints come from the controlled-source seismology (Choi et al., 2013; Liu et al., 2005; Song et al., 2007; Zhang et al., 2002). A series of explosions were recorded along two profiles approximately north-south and east-west in China (see for details of the experiment Song et al., 2007; Zhang et al., 2002). In the original work, Zhang et al. (2002) and Liu et al. (2005) identified low P wave velocities (< 5.9 km/s) and high Poisson's ratios (> 0.30) deeper than ~8 km depth, directly beneath CMP, interpreted as a number of "magma chambers" in the crust. However, a reanalysis of the same data suggested that the multiple chambers may be an artifact and that, while low velocities are present beneath CMP, the lowest velocities (> 5.4 km/s) were located north of CMP (Song et al., 2007). Choi et al. (2013) investigated this discrepancy and, while care must be taken due to the nonuniqueness inherent in modeling gravity data, suggested that the model of Zhang et al. (2002) is supported by regions of low density and the high conductivities identified by magnetotelluric studies (Qiu et al., 2014; Tang et al., 2001). However, the multiple magma chambers suggested by Zhang et al. (2002) are more likely explained by a distributed region of partial melt throughout the crust, as suggested by petrological studies at CMP (Andreeva et al., 2018; Pan et al., 2017) and similar to magma plumbing systems beneath other volcanoes (Annen et al., 2006; Cashman et al., 2017; Christopher et al., 2015; Sparks et al., 2019; Schmandt et al., 2019). More recently, a joint RF and surface wave study using data in China showed evidence for a significant low S wave velocity zone in the midcrust (~3.0 km/s), with high P wave to S wave ratio (> 1.8) directly beneath CMP, supporting evidence for the presence of a magma reservoir beneath the volcano (Zhu et al., 2019).

To investigate the crustal structure beneath and adjacent to the CMP, we present here the first analysis of a data set collected by seismometers deployed in both China and DPRK. The inclusion of this multinational data set allows us for the first time to estimate spatial distributions of melt on all sides of the volcano (Figure 1). We use RFs to map out spatial variations in crustal thickness, V_P/V_S, and intracrustal low-velocity zones, revealing the depth and lateral extent of zones of partial melt in the crust beneath the CMP and adjacent volcanoes.

2. Data and Methodology

We use data from six broadband seismometers deployed from August 2013 to August 2015 in the DPRK by the Mount Paektu Geoscientific Group (MPGG), a collaboration between DPRK, U.K., and U.S. scientists (Hammond, 2016; The Mount Peaktu Geoscientific Group (MPGG), 2013). We improve on a previous study that used 1 year of data from the six DPRK stations (Kyong-Song et al., 2016) by including the full 2-year data set. We also include data from five stations deployed in 1998 as part of a northeast China regional array (Wu, 1998), which provided between 2 and 7 months of data. New data come from temporary deployments and permanent stations (20 stations) run by the China Earthquake Administration (CEA). The permanent stations belong to the CEA national network, and 2 years of data (2011–2012) were provided for this study. The temporary CEA stations were deployed in the summer months (June–September) in the period 2002–2006 in response to the unrest at CMP (Xu et al., 2012; Wu et al., 2007). Many of these stations were deployed in spatial clusters to provide accurate earthquake locations (see for details Wu et al., 2002, 2007) and have been grouped for the purposes of our RF study. Where we have done this, we have calculated a mean position for plotting H-κ stacking results, but actual station latitudes and longitudes are used for migration of the RF. All station details can be found in Table 1. While RF studies have used the MPGG and northeast China array data previously, this is the first time a consistent cross-border study has been conducted. Further, previous studies on the Chinese side of the volcano using the northeast China array (Hetland et al., 2004) based their analysis on few data (one to seven RFs for the stations also used in this study). Adding the full MPGG data set and the permanent and temporary CEA data has significantly improved coverage beneath CMP, particularly in China (Figure 1).

It has been noted that some CEA permanent seismic stations are prone to variable misorientations (i.e., their north component is not oriented to true north) (Niu & Li, 2011). To account for this, we perform a principal component analysis on the P wave particle motion for all CEA stations to estimate misorientations

Table 1
Details of Seismic Stations Used in This Study

Station	Instrument type	RF grouping	Latitude °N	Longitude °E	Elevation (km)
Network: CEA Permanent					
CBS	BBVS	North	42.07	128.07	1.79
CBT	ESP	CBT and FROG	41.42	128.17	0.76
FST	ESP	—	42.26	127.38	0.77
MJT	BBVS	MJT and MANG	41.95	127.59	0.86
SMT	FSS	—	42.19	128.17	1.15
ZXT	FSS	ZXT and EDO	42.41	128.11	0.77
CEA Temporary					
DZD	BKD	North	42.06	128.06	1.77
HSZ	BKD	North	42.05	128.06	1.88
TC1	BKD	North	42.04	128.07	2.32
TC2	BKD	North	42.05	128.07	1.99
SM2	BKD	East	42.02	128.26	1.41
SM4	BKD	East	42.03	128.26	1.41
SMB	BKD	East	42.05	128.25	1.40
WD1	BKD	South	41.99	128.01	2.24
WD2	BKD	South	41.99	128.02	2.22
WD3	BKD	South	41.97	128.00	1.75
WD7	BKD	South	41.94	127.99	1.64
WD8	BKD-	South	41.94	128.01	1.67
WQD	BKD	North	42.04	128.06	1.89
EDO	BKD	ZXT and EDO	42.42	128.10	0.71
Network: MPGG					
JGPD	ESP	—	41.99	128.08	2.65
PDBD	40T	—	41.99	128.13	2.16
MDPD	ESP	—	41.97	128.20	1.80
SMSD	ESP	—	41.97	128.32	1.44
PSRD	40T	—	41.94	128.62	1.10
SHRD	ESP	—	41.95	128.79	1.04
Network: NE China					
CBAI	3T	North	42.06	128.06	1.82
CANY	3T	South	41.95	128.00	1.71
FROG	3T	CBT and FROG	41.42	128.17	0.80
MANG	3T	MJT and MANG	41.95	127.59	0.82
WUSU	3T	—	42.33	127.28	0.47

Note. RF grouping refers to joint analysis of seismic stations for the RF analysis. Instrument type refers to the following sensors and dominant periods: 3T = Guralp 3T sensor (120 s), ESP = Guralp ESP sensor (60 s), 40T = Guralp 40T sensor (30 s), BBVS = Beijing Gangzhen Instrument Ltd BBVS-60 sensor (60 s), FSS = Beijing Gangzhen Instrument Ltd FFS-3DH sensor (2 s), BKD = Institute of Geophysics, China Earthquake Administration BKD-2 Sensor (20 s).

(see Di Leo et al., 2015, and supporting information Text S1 and Figures S1–S5 for details). For the permanent stations, we use *P* waves from teleseismic events, but for most of the CEA temporary stations we take advantage of the local seismicity recorded beneath the volcano. The CEA temporary stations were removed and redeployed annually, so we recalculate the orientations accordingly. Due to the dense seismic networks deployed, errors in the local earthquake locations are less than 1 km (Wu et al., 2002, 2007). These errors could still introduce errors into the misorientation estimates, but the consistent azimuths estimated for all
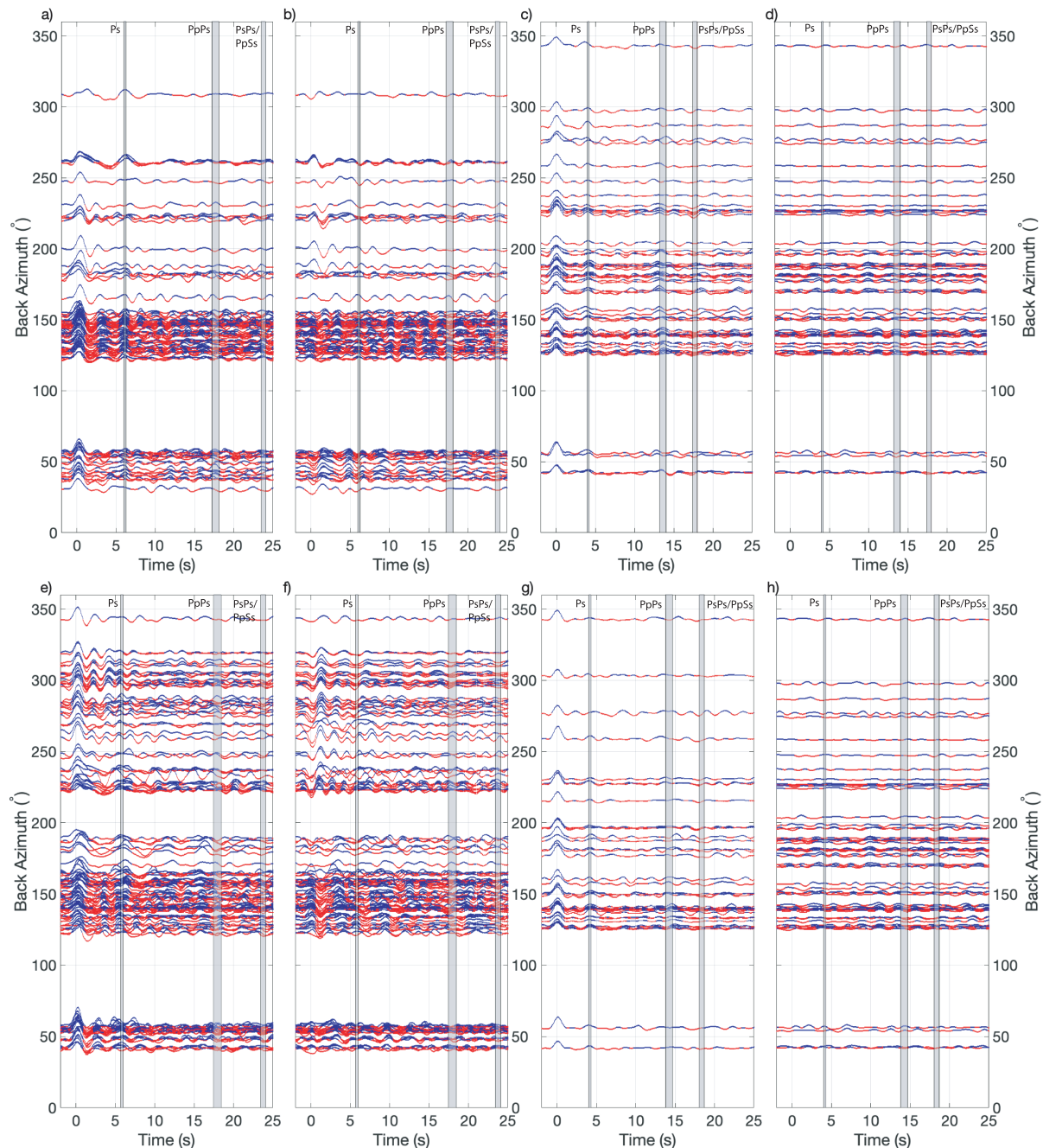
Figure 2. Receiver functions for (a, b) PDBD, (c, d) FST, (e, f) North group of stations and (g, h) MJT and MANG. (a, c, e, g) Radial component and (b, d, f, h) transverse component RF. Blue peaks show positive amplitude, and red show negative amplitude. Gray bars show approximate region of expected *Ps* phase arrival based on the stations *H-κ* solution.

events (Figures S2–S5) suggests that random errors have limited effect. A systematic error in location could cause a consistent error in the azimuth, but the fact that RFs estimated from corrected data appear to have most energy on the radial compared to transverse components Figures 2 and S6–S16) suggests that any effect is small. Local seismicity had reduced significantly by summer 2005, so we use teleseismic data to estimate orientations at some stations recording in 2005. Table S1 shows results for all stations.

To estimate RFs, we use teleseismic earthquakes greater than 5.5 M_w and with epicentral distances between 30° and 90°. We manually calculate the RFs using the extended-time multitaper technique (Helffrich, 2006), with a frequency domain low-pass cosine taper applied with a 1.0 Hz cutoff frequency that acts as a low-pass

Table 2
H-κ Stacking Results

| Station	H (km)	V_P/V_S	V_P (km/s)	NRF
CBT and FROG	36 ± 1	1.71 ± 0.01	6.5	82 (8, 15, 27, 32)
East	35 ± 1	1.92 ± 0.05	6.5	40 (5, 3, 12, 20)
FST	34 ± 1	1.74 ± 0.01	6.5	65 (7, 15, 21, 22)
JGPD	—	—	6.2	119 (20, 13, 56, 30)
MDPD	39 ± 1	1.89 ± 0.06	6.2	45 (3, 5, 23, 14)
MJT and MANG	36 ± 1	1.71 ± 0.02	6.5	42 (5, 15, 14, 8)
North	41 ± 2	1.84 ± 0.04	6.2	145 (14, 28, 47, 56)
PDBD	40 ± 1	1.93 ± 0.02	6.2	107 (25, 11, 44, 27)
PSRD	36 ± 1	1.76 ± 0.03	6.5	40 (5, 5, 18, 12)
SHRD	34 ± 1	1.81 ± 0.02	6.5	112 (16, 11, 48, 37)
SMSD	36 ± 3	1.84 ± 0.07	6.5	54 (7, 7, 27, 13)
South	37 ± 1	1.88 ± 0.05	6.2	53 (5, 5, 10, 33)
SMT	36 ± 1	1.78 ± 0.03	6.5	47 (4, 6, 20, 17)
WUSU	33 ± 1	1.71 ± 0.06	6.5	5 (1, 2, 1, 1)
ZXT and EDO	34 ± 1	1.73 ± 0.03	6.5	58 (7, 10, 19, 22)

Note. NRF is the number of receiver functions included in the stack. Numbers in brackets relate to the number of receiver functions with slownesses between 0.04 and 0.05 s/km, between 0.05 and 0.06 s/km, between 0.06 and 0.07 s/km, and between 0.07 and 0.08 s/km, respectively. These are used to weight the grid search inversions. No stable *H-κ* solution was observed for JGPD.

filter. We retain for further analysis those RF that meet the following criteria: (i) an approximate delta function on the vertical component; (ii) little presignal energy on the radial or vertical components; and (iii) no long period noise in the radial and transverse components. All RF data are shown in Figures 2 and S6–S16. Our results are consistent with RFs reported in previous studies (e.g., Kyong-Song et al., 2016), with simple RFs with clear Moho *Ps* and reverberated phases for stations far from the volcano (e.g., FST, MJT, and MANG) in both DPRK and China and more complex waveforms for those closer (e.g., PDBD, north group of stations) (Figures 2 and S6–16).

Following Kyong-Song et al. (2016), we first perform *H-κ* stacking (Zhu & Kanamori, 2000) to estimate the bulk crustal structure beneath our seismic stations and then perform common conversion point migration (Angus et al., 2006; Hammond et al., 2011) of the RF data to obtain a more detailed spatial image. Further, we perform simple grid search inversions (Lodge & Helffrich, 2009) and harmonic analysis (Schulte-Pelkum & Mahan, 2014) to test the hypothesis that intracrustal low-velocity zones associated with partial melt are present beneath CMP.

3. *H-κ* Stacking

The most common phases identified in *Ps* RF are the *P* wave to *S* wave conversion (*Ps*) from the Moho and three reverberations that bounce once at the surface, converting from a *P* wave to an *S* wave at some point along their path (*PpPs*, *PpSs*, and *PsPs* phases, where *P* and *S* are upgoing and *p* and *s* are downgoing *P* and *S* waves). The arrival times of these phases depend on the Moho depth, the average *P* wave and *S* wave velocity in the crust, and slowness (see for details Zhu & Kanamori, 2000). We know the slowness of the incident seismic wave and estimate the average *P* wave velocity from nearby controlled-source experiments carried out in China (Zhang et al., 2002) (Table 2). This leaves the crustal thickness (*H*) and *P* wave to *S* wave velocity ratio (V_P/V_S or *κ*) as unknowns. The *H-κ* stacking technique grid searches over *H* and V_P/V_S to find the solution that best predicts the times of the reverberated phases, identified by the point where energy at these times sums coherently. Here, we search over a range of crustal thicknesses from 25–45 km with intervals of 0.25 km and a V_P/V_S range of 1.7–2.2 with intervals of 0.00625. All three phases are weighted equally in the stack. The method assumes horizontal isotropic layers, which can introduce azimuthal variations in the receiver functions (Dugda et al., 2005; Hammond, 2014). We estimate errors by using a bootstrap method
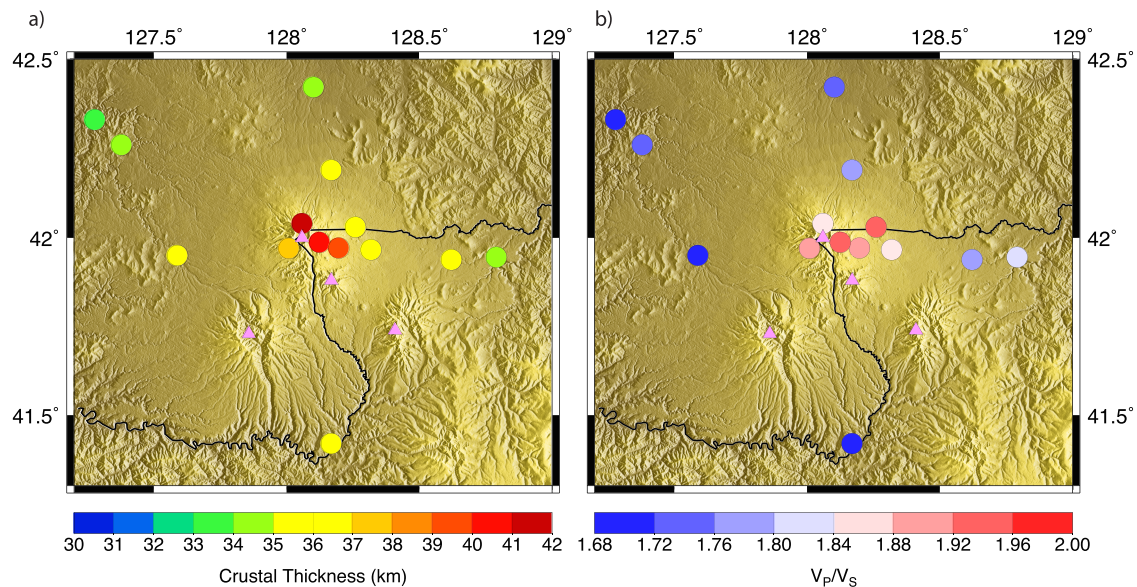
Figure 3. Map of (a) crustal thickness and (b) V_P/V_S ratio around Changbaishan/Paektu volcano. Triangles indicate volcano locations (see Figure 1 for details).

in which the data are resampled 2,000 times, with a random subset of the data selected each time for the H-κ stacking. The standard deviation of these 2,000 estimates gives the error. We also check the sensitivity to uncertainty in the average P wave velocity by varying it by 0.1 km/s. We then select the largest error from these two approaches to characterize uncertainty in our estimates.

H-κ stacking estimates in DPRK and China are consistent with previous results (Hetland et al., 2004; Kyong-Song et al., 2016). Far from the volcano, we find crustal thicknesses of ∼33–36 km with V_P/V_S of 1.7–1.8, typical for continental crust. The lowest values ($V_P/V_S < 1.74$) are found to the west of CMP (Table 2 and Figure 3). Near the volcano, the H-κ stacking results are more complex, showing an increase in V_P/V_S and two possible solutions (Figures S17–S20). Both solutions imply a higher than normal V_P/V_S (>1.84), but the solution with very high V_P/V_S (1.96–2.11) shows a slight thinning of the crust, while the lower V_P/V_S shows a thickening of crust. We follow the arguments outlined in Kyong-Song et al. (2016), who suggest only one of these solutions is correct due to the lack of a corresponding complex signal in the lower crust. While it is tempting to choose the solution that has the highest stack, in this case the higher V_P/V_S and thinner crust, the RF method is inherently nonunique meaning this may not be appropriate. Rather, to determine which is more likely we rely on previous studies using multiple data sets such as RFs (Hetland et al., 2004; Kyong-Song et al., 2016), controlled-source (Liu et al., 2005; Song et al., 2007; Zhang et al., 2002) and surface waves/seismic noise interferometry (Kim et al., 2017; Zhu et al., 2019). While these studies disagree on aspects of the internal crustal structure, all agree that a thicker crust is present beneath the volcano compared to surrounding regions. As a result, we suggest that the solution with thicker crust and slightly lower V_P/V_S is the more likely, and this is the solution we take going forward. These V_P/V_S are higher than would be expected for a mafic crustal composition (Christensen, 1996) and similar to that seen in other volcanic areas (e.g., Ethiopia, Dugda et al., 2005; Hammond et al., 2011; Stuart et al., 2006 and Italy Piana Agostinetti & Amato, 2009), interpreted as partial melt in the crust. Additionally, a thicker than normal crust is often found beneath volcanic areas linked to the intrusion of mafic material into the lower crust (e.g., Ethiopia, Ebinger et al., 2017, Azores, Ramalho et al., 2017, and Faroe Islands, White et al., 2008).

4. Harmonic Analysis

There exists clear energy with 360° periodicity in the first few seconds on the transverse components at stations close to the volcano (Figure 2). This is well recognized to be due to either a dipping layer or anisotropy with a dipping symmetry axis (Eckhardt & Rabbel, 2011; Levin & Park, 1998; Savage, 1998; Schulte-Pelkum & Mahan, 2014). To investigate this further, we follow the approach outlined by Schulte-Pelkum and Mahan (2014). They show that the radial and transverse components can be combined to facilitate a simple
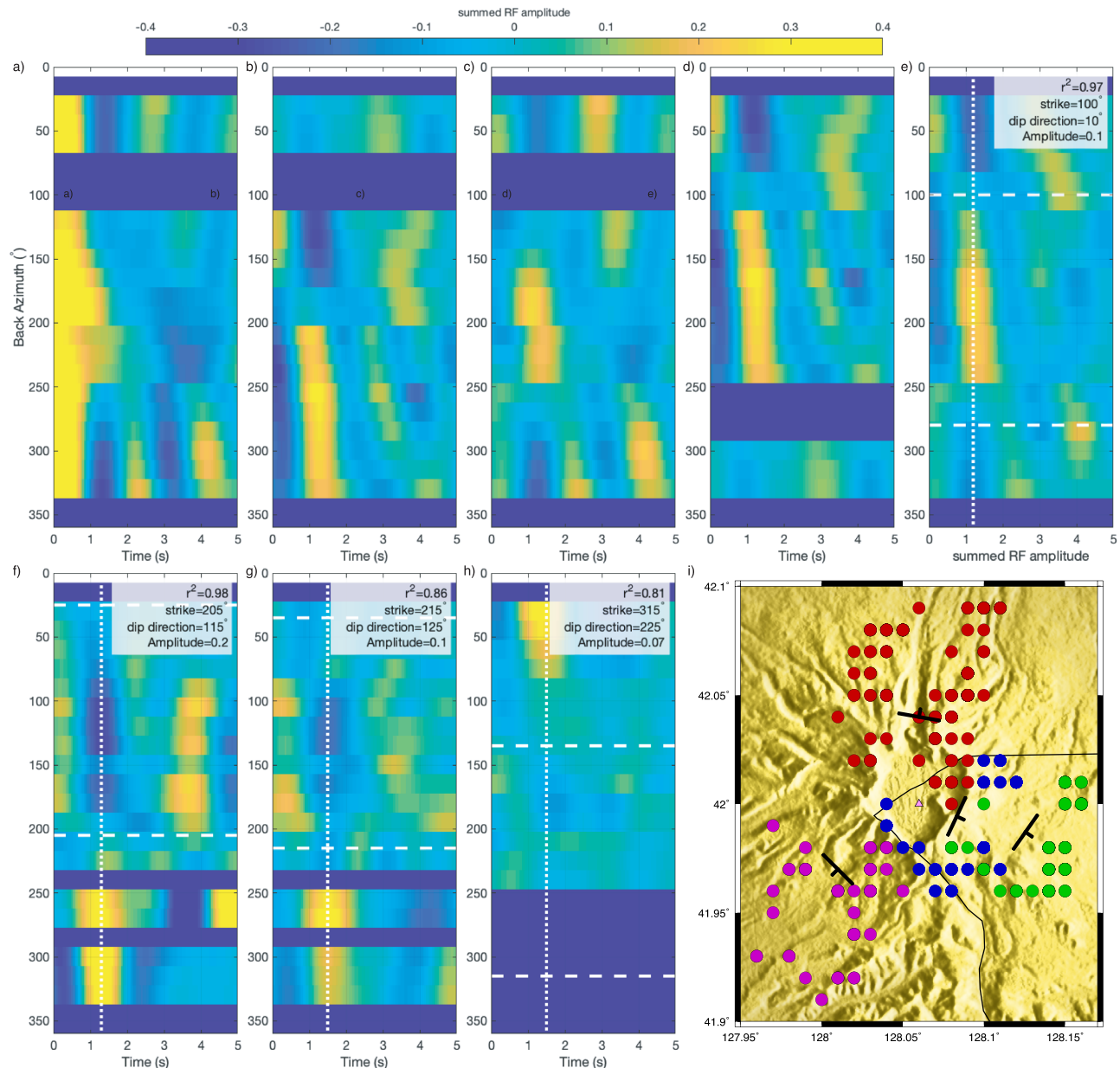
Figure 4. Harmonic analysis to estimate a dipping/anisotropic crust. (a–e) Different stages for the north group of stations (see text for details). (a) Radial receiver functions binned into 30° stacks overlapping by 15° each side. (b) Transverse receiver functions binned into 30° stacks overlapping by 15° each side. (c) Corrected radial receiver functions showing radial receiver function minus the mean energy across all azimuths at each time sample. (d) Transverse receiver functions shifted by 90°. Note the similarity in signal in (c) and (d). (e) The summed receiver function, where data in (c) and (d) are added. These data undergo harmonic analysis. The white dashed line shows the strike of the best fitting (360° periodicity) harmonic. White dotted line shows the time with maximum RF amplitude. Also shown are the results of the harmonic analysis for (f) JGPD, (g) PDBD, and (h) south group of stations. (i) Strike and dip direction for the four stations close to the volcano. Colored circles show piercing points at ~7 km depth for each station (red = north group; blue = JGPD; green = PDBD; and magenta = south group).

harmonic analysis (Figure 4). We stack the RF data into 30° back azimuth bins with a 15° overlap each side and use these stacked data for the harmonic analysis (Figures 4a and 4b). The first step is to remove the mean radial RF amplitude across all back azimuths from the radial RF (Figure 4c). This produces data with a harmonic signal similar to the transverse component; however, the radial and transverse RF are now out of phase by 90° (Figure 4b). To make these more comparable, we shift the transverse component by 90° (Figure 4d) and finally sum the radial component with mean removed and shifted transverse component to produce the final harmonic signal (Figure 4e). We perform a simple harmonic analysis on this stacked trace

Table 3
Harmonic Analysis Results

Station	Strike (°)	Dip direction (°)	Average RF amplitude	r^2 value
CBT and FROG	330	240	0.03	0.88
East	115	25	0.03	0.87
FST	185	95	0.02	0.89
JGPD	**205**	**115**	**0.20**	**0.98**
MDPD	140	50	0.03	0.77
MJT and MANG	120	30	0.02	0.26
North	**100**	**10**	**0.10**	**0.97**
PDBD	**215**	**125**	**0.10**	**0.86**
PSRD	140	50	0.02	0.95
SHRD	240	150	0.02	0.76
SMSD	335	245	0.02	0.86
South	**315**	**225**	**0.07**	**0.81**
SMT	215	125	0.03	0.93
ZXT and EDO	125	35	0.02	0.95

Note. Station names in bold show evidence for a dipping layer within the crust, with strong average RF amplitude > 0.03 and a r^2 value > 0.8.

to find the best fitting strike (defined by the zero crossings in the data) (Figure 4e) for the signal between 1 and 2 s. We constrain the goodness of fit by calculating the r^2 value between the best fitting harmonic and the amplitude of the summed RF, and we get an estimate of the strength of the signal by estimating the average absolute amplitude of the summed RF across times associated with the harmonic signal. We take all values with an $r^2 > 0.8$ and an amplitude > 0.03 as being indicative of a dipping or anisotropic layer.

The strike of this signal defines either the strike of a dipping layer or the plane perpendicular to the symmetry axis for dipping anisotropy (the foliation plane for a symmetry axis defined by the slow axis as would be expected in the crust). Schulte-Pelkum and Mahan (2014) suggests that harmonic signal at 0 s on the transverse component can be used to distinguish between these models. This signal will be present for an isotropic dipping layer due to any *Ps* conversion at a dipping plane resulting in *P* wave energy out of the radial plane, but will not be present for anisotropy (unless anisotropy is present all the way to the surface). This signal is present in our data suggesting a dipping layer is present within the crust. This allows us to determine the direction of the dip, which is defined by the largest amplitude signal on the radial component as events traveling updip will arrive at a low incidence angle, resulting in a stronger *P* to *S* wave conversion.

The four stations closest to the volcano (the north group, southwest group, JGPD, and PDBD) show strong evidence for a dipping layer in the upper crust (Table 3 and Figure 4) and are associated with a strong negative peak on the radial component showing that this discontinuity is associated with a velocity reduction with depth. Dip directions are all oriented away from the volcano (Figure 4), suggesting that the low-velocity feature is shallowest beneath the volcano. The harmonic analysis for all other stations can be found in Table 3 and Figures S21–S33.

5. Grid Search Inversion

The harmonic analysis shows evidence for a velocity reduction with depth in the crust beneath CMP. To understand the spatial extent of this feature, we perform a simple grid search inversion. We follow the approach outlined by Lodge and Helffrich (2009), who argued that in the presence of reasonable *a priori* information, this grid search technique can fit models with similar complexity to the data. Thus, this approach is useful to test the simple hypothesis that a low-velocity layer is present in the upper crust. While there is evidence for dipping layers in the crust associated with the velocity reduction, the modeling approach here assumes isotropic horizontal layers. This limits the ability to interpret the strength of the velocity reduction, but it is useful in determining at which stations a velocity reduction in depth is required

by the data. To see the effect this has on the data, we model updip and downdip RFs separately for the north group of stations by including data within 60° of the up or downdip direction. For all other stations we include all data in the stack. For stations JGPD, PDBD, and the south group, which show evidence for dipping layers, the model can be assumed to be related to events traveling updip, as these azimuths dominate the stack.

For our initial model, we construct a simple three-layer model based on the nearby controlled-source experiments (Zhang et al., 2002). We include one shallow layer representing relatively low velocity tephra and sediment, lava flows, and consolidated volcanic rocks (Vanorio et al., 2002). We assign to this layer a gradational velocity increase defined by its thickness and the velocities and V_P/V_S ratios at the surface and in the layer below. The second and third layers have velocities typically associated with the upper crust, with the difference that Layer 3 can have lower or higher velocities than Layer 2. We vary V_P/V_S and P wave velocity for all three layers and thickness for the upper two layers (see Table S2 for details on the parameter space). As we are modeling the upper crust only, we estimate density in all layers using the empirical density-P wave velocity relationship for the upper crust of Christensen and Mooney (1995) (ρ ($kg\,m^3$) $= 989.3 + 289.1\,V_P$). In total, we produce 358,935 models for each station. We generate four synthetic RFs for variable slowness ranging from 0.045–0.075 s/km in steps of 0.01 (roughly equivalent to epicentral distances of 35–85°). We stack the RF, weighting each by the distribution of slownesses present in the real data (Table 2). This is important as slowness strongly influences the amplitude of the initial P wave arrival on the radial RF and thus the fit to the data.

We estimate the misfit between observed and modeled RF by estimating the χ^2 value, given by

$$\chi^2 = \sum \frac{(RF_D(i) - RF_S(i))^2}{\sigma_i^2}, \tag{1}$$

where RF_D and RF_S are the observed and synthetic RF, respectively, and σ is the jackknife estimated 2σ standard deviation of the observed RF. We focus our model on the internal crustal structure alone and thus do not attempt to fit the Ps conversion from the Moho. As a result we only estimate the misfit in the first few seconds before the inferred Moho Ps conversion is observed (Figure 5). The only exception to this is station JGPD, which had no clear H-κ stacking solution. In this case we focus on the strong negative peak in the first 4 s. We resample our data at 2.5 Hz so as to fit only the number of data points needed to fully represent the RF (Figure S34) (the maximum frequency content of the RF is 1 Hz). In the case that the synthetic RF exactly matches the observed, $\chi^2 = 0$. However, given the error in the data, a suitable threshold value must be chosen, and we select a $\Delta\chi^2$ value determined by the number of degrees of freedom (ν) in the model. To test models with a low-velocity layer in the crust, we vary eight parameters and so at 95 % confidence the $\Delta\chi^2 = 15.51$ (we also show results for 99 % confidence where $\Delta\chi^2 = 20.09$ in Figure 5). We assume that any χ^2 value less than that for 95% confidence represents a reasonable fit to the data.

Figure 5 shows all those models that fit the data within these criteria. Rather than focus on the absolute velocities, which RF are relatively insensitive to, we plot velocity contrast between Layers 2 and 3 for all models. The first few seconds of RFs at almost all stations can be explained by the presence of a simple sedimentary structure, with no requirement for a low-velocity zone in the crust. However, for those stations closest to the summit of CMP (north group, south group, JGPD, PDBD), the model indicates a strong S wave velocity reduction in the upper crust (32–37% at 4–5 km (JGPD), 11–22% at 4–5 km (south group), 5–26% at 6–8 km (north group [updip]) and 3–18% at 5-8 km (PDBD), where all depths are below sea level). While these models show that a velocity reduction with depth is present at 4–8 km depth, the absolute velocity reduction must be considered an overestimate as most arrivals are traveling updip, enhancing the amplitude of the signal. This is best shown by the contrast in velocity models for events arriving updip or downdip at the north group of stations. Those arriving updip show a strong velocity reduction, while those traveling downdip show no reduction in velocity.

6. Common Conversion Point Migration

H-κ stacking provides a single estimate of crustal structure for each station and shows that the volcano sits on thick crust with high average V_P/V_S throughout the crust (Figure 3). The grid search inversions suggest a
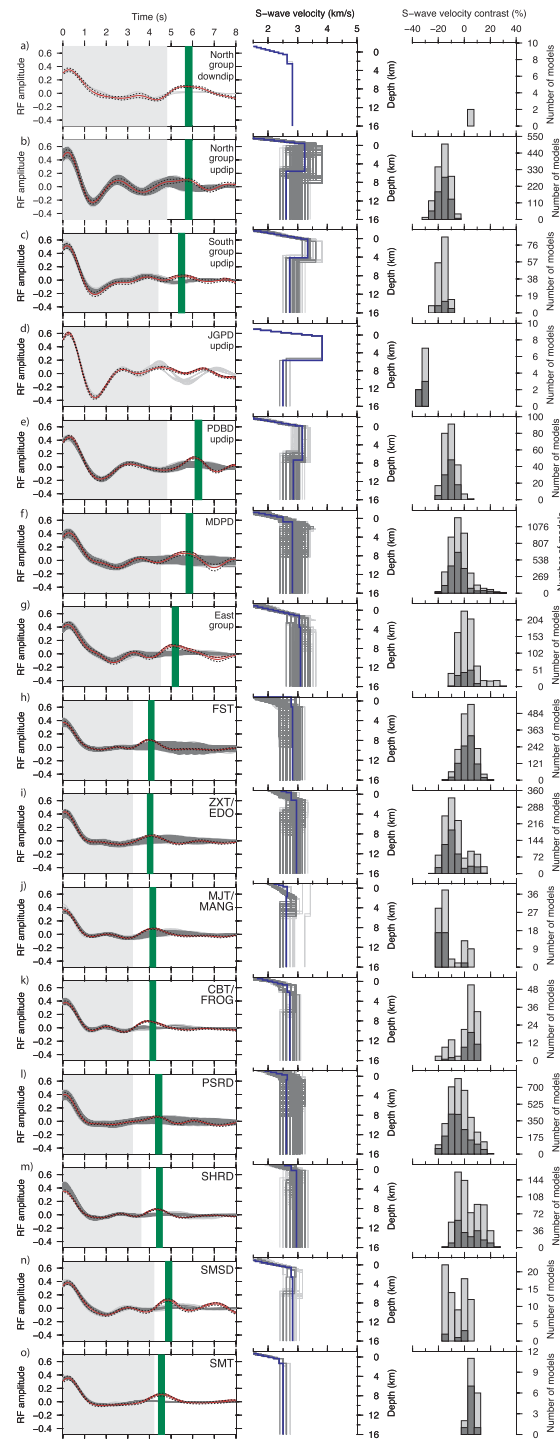
Figure 5. Inversions to constrain upper crustal velocity discontinuities. Left plots show observed stacked RF (red solid line) and 95% jackknife confidence intervals (black dashed lines) and synthetic RF. The light gray area shows the portion of the RF that is included in the misfit calculation. The green bar shows expected arrival times for a *Ps* conversion from the Moho, based on *H-κ* stacking results (Table 2). Middle plots show all *S* wave velocity profiles for those models that statistically fit the RF data with the blue profile showing the velocity model used to generate synthetic RF in the CCP migration. All depths are relative to sea level. Right plots show histograms for all velocity contrasts for the bottom two layers in all models that statistically fit the RF data. In all plots, dark gray and light gray lines/bars relate to those models that fit below the 95% and 99% $\Delta\chi^2$ misfit value. (a) North group (events traveling downdip only), (b) north group (events traveling updip only), (c) south group, (d) JGPD, (e) PDBD, (f) MDPD, (g) east group, (h) FST, (i) ZXT and EDO, (j) MJT and MANG, (k) CBT and FROG, (l) PSRD, (m) SHRD, (n) SMSD, (o) SMT.
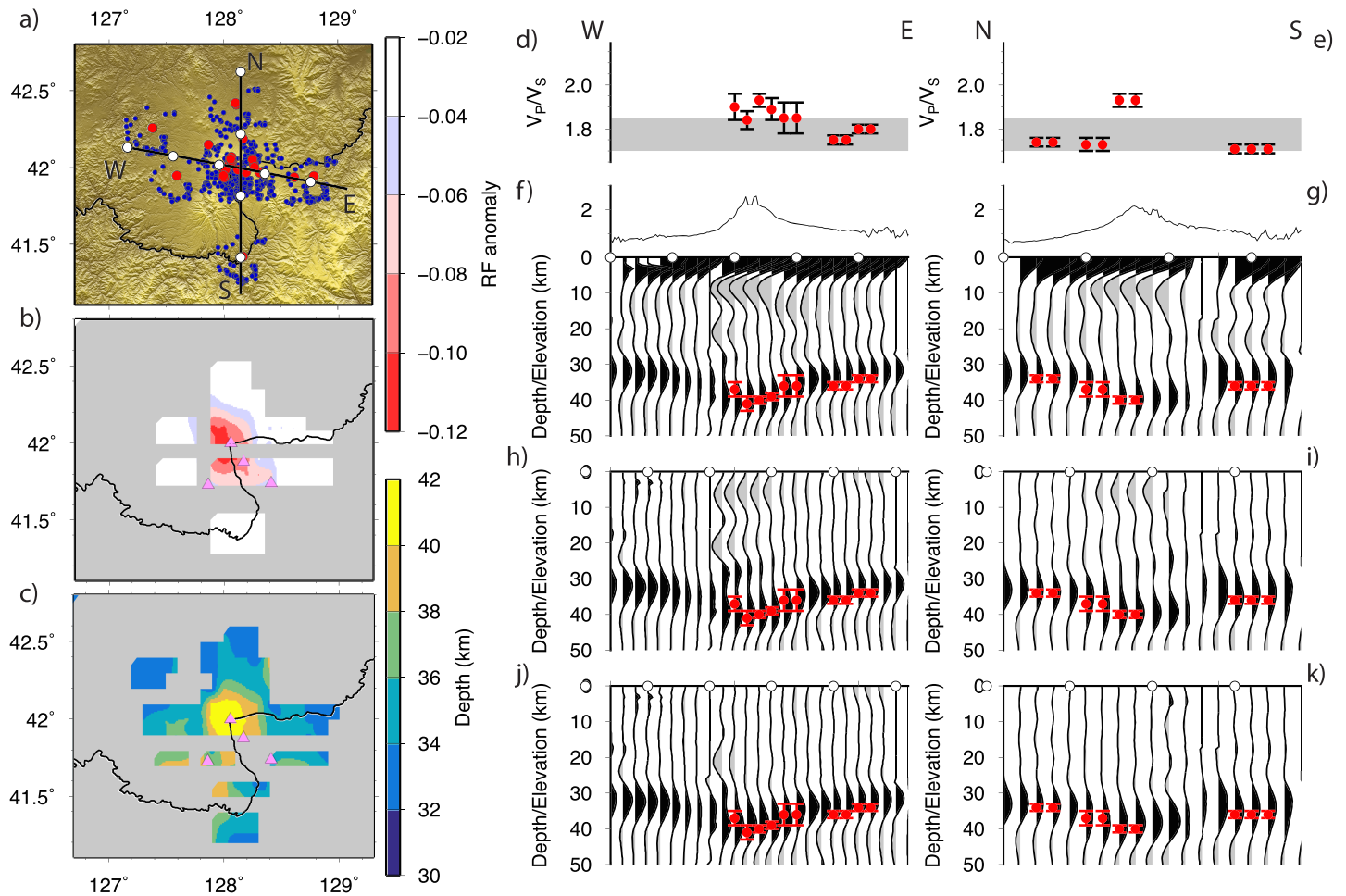
Figure 6. Common conversion point migrations. (a) Map showing profile lines and piercing points (blue circles) for a 35 km thick crust and an IASP91 velocity model. (b) Map showing largest negative RF anomaly from the CCP migrations between 4 and 15 km depth. Note the strong anomaly directly beneath Changbaishan/Paektu volcano. (c) Estimates of Moho depth extracted from the CCP migration. Pink triangles show volcano locations (see Figure 1 for details). (d, e) *H-κ* stacking results for stations along the W-E and N-S profiles, respectively; (f, g) CCP migrations for original RF for the W-E and N-S profiles, respectively; (h, i) CCP migrations for RF corrected for shallow structure using the model shown in Figure 5 but excluding the low-velocity layer for the W-E and N-S profiles, respectively; (j, k) CCP migrations for the RF corrected for shallow structure using the model shown in Figure 5, including the low-velocity layer for the W-E and N-S profiles, respectively. Note the absence of structure in (h) and (i) except for the low-velocity zone beneath the volcano and the absence of any structure in (j) and (k) showing that this model can explain crustal structure well.

reduction in velocity is required at a depth of 4–8 km below sea level, and harmonic analysis suggests this is shallowest beneath the volcano. However, these techniques present an estimate for a single point assumed to be directly beneath the seismic station. In reality, the teleseismic events used to generate RF have different back azimuths and slowness, such that a much wider region of the crust is being sampled (Figure 1). To exploit this, we perform a common conversion point (CCP) migration, which attempts to place the RF energy at a point in a model where the conversion occurred (Angus et al., 2006). For each station we update the IASP91 velocity model by moving the Moho depth to that estimated from the *H-κ* stacking and calculating the *S* wave velocity using the IASP91 *P* wave velocity and V_P/V_S from the *H-κ* stacking. This means that each station has its own velocity model (Hammond et al., 2011). Ideally we would perform 3-D ray tracing, but to date, largely due to a lack of data on all sides of the volcano, no suitable velocity model exists. We account for topography, so that all migrations are shown with respect to sea level. The model is discretized into bins, where amplitudes are averaged within a given distance with a radius defined by the Fresnel zone so that bins increase with depth. We impose a minimum bin radius of 5 km. We only show bins that have a minimum of five hits per bin.

Kyong-Song et al. (2016) showed CCP migrations along a single east-west profile beneath DPRK, revealing a thick crust beneath the volcano with large negative peaks suggesting strong velocity reduction at

5–10 km depth. We can now extend this profile to the Chinese side of the volcano and investigate north-south heterogeneity (Figure 6). We find a thick crust and a strong negative peak beneath CMP, supporting the identification of a low-velocity layer directly beneath CMP from the grid search inversions (Figure 5). To improve resolution of the low-velocity zone, we generate synthetic seismograms to correct for the shallow sedimentary structure. This is a similar technique to that commonly applied in RF studies in Antarctica where the effects of the ice thickness on RF are modeled to try and image deeper (e.g., Anandakrishnan & Winberry, 2004; Chaput et al., 2014). For each station-teleseismic event pair used to generate an RF, we use the velocity model constrained by the inversions for each station and the slowness of each teleseismic event to generate a synthetic RF. We subtract the synthetic RF from each observed RF before migrating the remaining RF energy in depth. For those stations that do not require a low-velocity zone, we use all three layers in the velocity model to generate the synthetic RF. For those stations where a low-velocity zone is seen in the grid search inversions, we use only the top two layers in the velocity model to generate the synthetic RF. For the north group of stations we use the relevant velocity model for those events traveling up or downdip. This has the effect of removing all shallow structure from the RF, including the direct *P* wave arrival but leaving the energy associated with the velocity reduction at 4–8 km depth.

The grid search inversions highlight the nonuniqueness of the RF. For some stations, such as the north group, south group, or PDBD, the models are normally distributed around a single model. However, for others, such as MJMA, a bimodal distribution is observed (Figure 5). In this case, the data can be explained by both the absence of a low-velocity layer or by a significant velocity reduction with depth. It may seem logical to choose the model with the smallest misfit, but statistically all models that fit the data within the 95% confidence bounds can be considered good fits to the data. Rather, we appeal to Occam's Razor and choose the best fitting model that requires no low-velocity zone unless demanded by the data (stations JGPD, PDBD, the north group, and the south group only) (Figure 5). After removal of the shallow structure, including the *P* wave arrival, the migrations are much clearer preserving the negative peak associated with the velocity reduction at 4–8 km depth and the positive peak associated with the Moho (Figure 6). If we include all three layers at all stations when generating the synthetic RF before subtracting these from the data, we remove almost all pre-Moho conversion energy showing that this model explains the intercrustal RF data well (Figure 6). We also perform a migration of the data corrected using models with the lowest misfits. This produces similar results with a strong velocity reduction with depth beneath the volcano but has significant velocity reductions over a much wider region (Figure S35).

The benefit of our approach is that by removing the effects of sediment reverberations, we can confidently map out the spatial distribution of the low-velocity region beneath CMP. We search our CCP migrations for the strength of the negative peak and plot this in Figure 6b. This shows that the velocity reduction is present directly beneath CMP. Analysis of the strength of this anomaly should be avoided as we have not corrected for the effects of the dipping layer. For example, the largest anomalies are in the north/northwest, which may be caused by events traveling updip to the north group of stations. However, it shows that significant anomaly extends ~30 km to the north and east. This is compatible with previous delineation of a region of low velocities and high conductivities in China (Qiu et al., 2014; Tang et al., 2001; Zhang et al., 2002). There is a suggestion that a low-velocity zone is present beneath nearby volcanoes in DPRK and China (Figure 6b), but our data coverage in these regions is limited. We also map out Moho topography in the CCP migrations revealing in more detail the thickened crust directly beneath CMP.

7. Implications for the Magmatic System Beneath CMP

The best constraints on the crustal magmatic system beneath CMP come from petrology. Focussing mainly on the deposits of 946 CE eruption, these studies suggest multiple regions of magma storage in the crust (Andreeva et al.,2018; Iacovino et al., 2016; Liu et al.,1998; Pan et al., 2017 Ramos et al.,2016, 2019). They argue that an evolved magma storage region is present at depths of 2–4 km below sea level, where commendite and trachy-basalts mixed before erupting in 946 CE (Andreeva et al., 2018; Iacovino et al., 2016; Pan et al., 2017). A larger, more primitive magma reservoir is present deeper than this, providing longer-term storage for the magmatic system (Andreeva et al., 2018; Pan et al., 2017). To date, no geophysical survey has imaged or shown evidence for a shallow magmatic system linked to the evolved commendite storage, suggesting it is small and/or cool. However, this study and past geophysical surveys do show evidence for an anomalous deeper region of low velocities(Hetland et al., 2004; Kyong-Song et al., 2016; Liu et al., 2005;
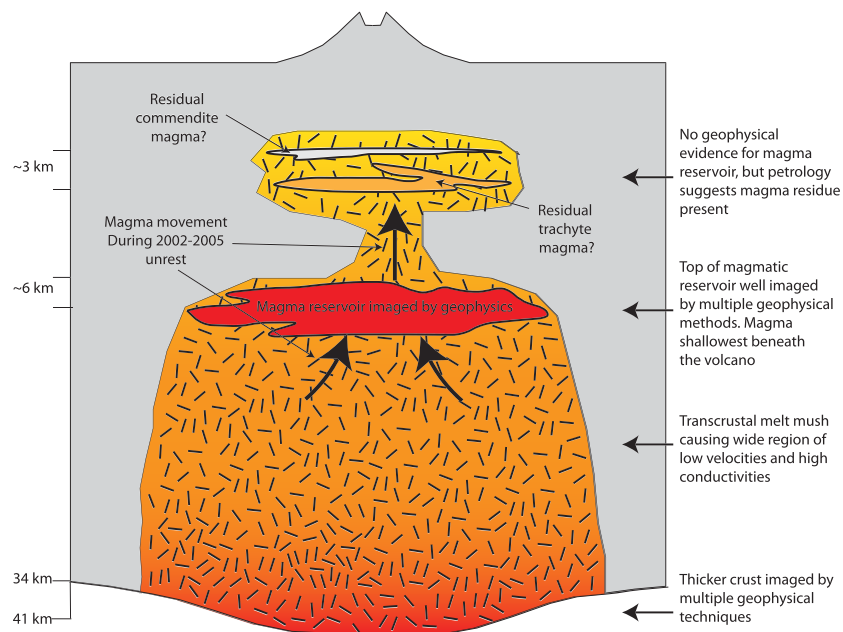
Figure 7. Conceptual model for the transcrustal magma plumbing system beneath CMP. Adapted from Pan et al. (2017).

Song et al., 2007; Wu et al., 2009; Yang et al., 2019; Zhu et al., 2019; Zhang et al., 2002), attenuation (Wu et al., 2006), and conductivity (Choi et al., 2013; Tang et al., 2001).

Previous geophysical studies have debated whether the anomalies require the presence of melt today. Song et al. (2007) argued that the low velocities computed in their model are likely due to a thermal anomaly rather than the presence of melt. They base this on relatively low Poisson ratios estimated from their RFs along with heat flow measurements from hot springs around CMP (Ehara et al., 2000). However, the prevalence of geophysical evidence such as high conductivities (Choi et al., 2013; Tang et al., 2001), strong velocity reduction (this study, (Zhang et al., 2002; Zhu et al., 2019), and strong attenuation (Wu et al., 2006) directly beneath the volcano suggest the presence of significant partial melt is likely. An exception to this is the study of Kim et al. (2017), who find little evidence for a velocity reduction with depth in the crust beneath CMP. They suggest that this precludes the presence of partial melt, showing that cooled magmatic intrusions are more likely. Our results are consistent with this, with V_P/V_S >1.8 across a wide region showing possible mafic addition to the crust. However, we show a relatively localized region with V_P/V_S >1.9 and low velocities in the crust directly beneath CMP, consistent with low velocities, high attenuation, and high conductivities seen in a similar location in many other studies (Hetland et al.,2004; Song et al.,2007; Zhang et al.,2002;Wu et al.,2006, 2009). A possible explanation for this difference is that the Kim et al. (2017) study has a lateral resolution in the crust greater than ~100 km. As a result, it is sensitive to the wider region of magmatic intrusion, but not the localized region of low velocities.

Further evidence for the presence of melt beneath the volcano today comes from similarities in major and trace elements and isotopic measurements for the 946 CE eruption and more recent eruption deposits (1668, 1781, 1811, and 1903 CE). This is interpreted to show that these eruptions have tapped the same magmatic source, suggesting trachyte magma has remained present beneath CMP for the last 2,200 years (Ramos et al., 2016). However, evidence for post-946 CE eruptions of the volcano is not universally accepted, with Pan et al. (2017) arguing that those interpreted as younger than 946 CE are rather reworked deposits from the 946 CE eruption itself. However, recent studies of sanadines in the proposed post 946 CE eruptions at 1668 and 1903 show ages younger than those associated with the 946 CE eruption (Ramos et al., 2019), suggesting more recent eruptions have occurred.

In this study, we show evidence that melt is likely as we see high average V_P/V_S for the whole crust and an S wave velocity reduction at 4–8 km below sea level, with shallowest depths beneath the volcano (Figure 7). In a seismic experiment conducted before the seismic unrest, Liu et al. (2005) estimated Poisson's ratios in the

crust of up to 0.3 ($V_P/V_S = 1.9$). In our inversions, the V_P/V_S exceeds 2.1 in the low-velocity layer beneath JGPD and is similarly high for other nearby stations. These high V_P/V_S and the velocity reduction beneath CMP are present at a depth comparable to that modeled for the inflation source during the 2002–2005 unrest (2–9 km) (Xu et al., 2012; Wei et al., 2013) and that suggested from post-unrest magnetotelluric measurements (∼5–8 km) (Qiu et al., 2014). This supports the hypothesis that basaltic melt recharged the magmatic system beneath CMP between 2002 and 2005.

While the top of this melt-rich region is well constrained, its base is not. This is best evidenced by the CCP migrations after correction for all shallow structure, including the low-velocity zone (Figure 6), where little structure is evident. This suggests that either partial melt is extensive throughout the crust or that a gradational layer is present at the base of the melt-rich region precluding imaging by the RFs. Previous estimates from seismic data and magnetotellurics imaged an extensive region of low velocities and high conductivities throughout the crust (Qiu et al., 2014; Tang et al., 2001; Zhang et al., 2002; Zhu et al., 2019). This suggests that, while the top of this region has a sharp boundary, the whole crust is likely warm and/or contains partial melt (Figure 7). This is also supported by the high average crustal V_P/V_S for the whole crust indicated by our H-κ stacking. This is similar to many volcanoes worldwide that show extensive magma reservoirs throughout the crust (e.g., Montserrat ; Christopher et al., 2015, Altiplano ; Ward et al., 2014; Comeau et al., 2015, Ethiopia ; Hammond, 2014and Iceland Hudson et al., 2017), including similar large silicic caldera volcanoes in the United States that show evidence for large, midcrustal (5–15 km depth) magma reservoirs (Schmandt et al., 2019).

8. Conclusions

We have computed RFs from teleseismic earthquakes recorded at seismic stations in both China and DPRK. This allows us to constrain the crustal structure and the spatial distribution of partial melt in the crust beneath all sides of the volcano. We show that the region close to CMP and extending ∼30 km from the summit has thick crust and high V_P/V_S and contains significant melt below 4–8 km below sea level, with shallowest depths directly beneath the volcano (Figure 7). The lack of a base to this melt-rich region suggests melt is pervasive throughout the crust, at least at the resolution we can achieve using teleseismic waves. Tantalizingly, we see similar thickened crust and evidence for shallow low velocities beneath neighboring volcanoes, hinting that they may also sit above magmatic systems. However, these areas lie at the limits of our data coverage, and further studies will be needed to test this hypothesis.

The velocity reduction and requirement for high V_P/V_S beneath the volcano lead us to suggest that the episode of unrest in 2002–2005 may have involved magma intrusion in to the magma storage region. This period of unrest did not lead to an eruption, but the evidence for an active magmatic system beneath CMP highlights the importance of sustained operational surveillance of the volcano.

References

Anandakrishnan, S., & Winberry, J. P. (2004). Antarctic subglacial sedimentary layer thickness from receiver function analysis. *Global and Planetary Change*, *42*(1-4), 167–176.

Andreeva, O. A., Yarmolyuk, V. V., Andreeva, I. A., & Borisovskiy, S. E. (2018). Magmatic evolution of Changbaishan Tianchi Volcano, China–North Korea: Evidence from mineral-hosted melt and fluid inclusions. *Petrology*, *26*(5), 515–545.

Angus, D. A., Wilson, D. C., Sandvol, E., & Ni, J. F. (2006). Lithospheric structure of the Arabian and Eurasian colliern Turkey from S-wave receiver functions. *Geophysical Journal International*, *166*, 1335–1346.

Annen, C., Blundy, J. D., & Sparks, R. S. J. (2006). The genesis of intermediate and silicic magmas in deep crustal hot zones. *Journal of Petrology*, *47*(3), 505–539.

Cashman, K. V., Sparks, R. S. J., & Blundy, J. D. (2017). Vertically extensive and unstable magmatic systems: A unified view of igneous processes. *Science*, *355*(6331), eaag3055.

Chaput, J., Aster, R. C., Huerta, A., Sun, X., Lloyd, A., Wiens, D., & Wilson, T. (2014). The crustal thickness of West Antarctica. *Journal of Geophysical Research: Solid Earth*, *119*, 378–395. https://doi.org/10.1002/2013JB010642

Choi, S., Oh, C.-W., & Götze, H.-J. (2013). Three-dimensional density modeling of the EGM2008 gravity field over the Mount Paekdu volcanic area. *Journal of Geophysical Research: Solid Earth*, *118*, 3820–3836. https://doi.org/10.1002/jgrb.50266

Christensen, N. I. (1996). Poisson's ratio and crustal seismology. *Journal of Geophysical Research*, *101*(B2), 3139–3156.

Christensen, N. I., & Mooney, W. D. (1995). Seismic velocity structure and composition of the continental crust: A global view. *Journal of Geophysical Research*, *100*(B6), 9761–9788.

Christopher, T. E., Blundy, J., Cashman, K., Cole, P., Edmonds, M., Smith, P. J., et al. (2015). Crustal-scale degassing due to magma system destabilization and magma-gas decoupling at Soufrière Hills Volcano, Montserrat. *Geochemistry, Geophysics, Geosystems*, *16*, 2797–2811. https://doi.org/10.1002/2015GC005791

Comeau, M. J., Unsworth, M. J., Ticona, F., & Sunagua, M. (2015). Magnetotelluric images of magma distribution beneath Volcán Uturuncu, Bolivia: Implications for magma dynamics. *Geology*, *43*(3), 243–246.

Di Leo, J. F., Wookey, J-M., Kendall, J.-M., & Selby, N. D. (2015). Probing the edge of the West African Craton: A first seismic glimpse from Niger. *Geophysical Research Letters*, *42*, 1694–1700. https://doi.org/10.1002/2014GL062502

Dugda, M. T., Nyblade, A. A., Julia, J., Langston, C. A., Ammon, C. J., & Simiyu, S. (2005). Crustal structure in Ethiopia and Kenya from receiver function analysis: Implications for rift development in eastern Africa. *Journal of Geophysical Research*, *110*, B01303. https://doi.org/10.1029/2004JB003065

Ebinger, C., Keir, D., Bastow, I., Whaler, K., Hammond, J. O. S., Ayele, A., et al. (2017). Crustal structure of active deformation zones in Africa: Implications for global crustal processes. *Tectonics*, *36*, 3298–3332. https://doi.org/10.1002/2017TC004526

Eckhardt, C., & Rabbel, W. (2011). *P*-receiver functions of anisotropic continental crust: A hierarchic catalogue of crustal models and azimuthal waveform patterns. *Geophysical Journal International*, *187*(1), 439–479.

Ehara, S., Jun, X., Fujimitsu, Y., Mogi, T., Itoi, R., Kai, T., & Zhang, L.-H. (2000). Crustal temperature and geothermal systems in the northeastern part of China. Proceedings world geothermal congress (pp. 2069-2073).

Hammond, J. O. S (2014). Constraining melt storage geometries beneath the Afar Depression, Ethiopia from teleseismic receiver functions: The anisotropic *H-κ* stacking technique. *Geochemistry, Geophysics, Geosystems*, *15*, 1316–1332. https://doi.org/10.1002/2013GC005186

Hammond, J. O. S (2016). Understanding volcanoes in isolated locations: Engaging diplomacy for science. *Science and Diplomacy*, *5*, 26–37.

Hammond, J. O. S, Kendall, J-M., Stuart, G. W., Keir, D., Ebinger, C. J., Ayele, A., & Belachew, M. (2011). The nature of the crust beneath the Afar triple junction: Evidence from receiver functions. *Geochemistry, Geophysics, Geosystems*, *12*, Q12004. https://doi.org/10.1029/2011GC003738

Hayes, G. P., Moore, G. L., Portner, D. E., Hearne, M., Flamme, H., Furtney, M., & Smoczyk, G. M. (2018). Slab2, a comprehensive subduction zone geometry model. *Science*, *362*(6410), 58–61.

Helffrich, G. (2006). Extended-time multi-taper frequency domain cross-correlation receiver function estimation. *Bulletin of the Seismological Society of America*, *96*, 344–347.

Hetland, E. A., Wu, F. T., & Song, J. L. (2004). Crustal structure in the Changbaishan volcanic area, China, determined by modeling receiver functions. *Tectonophysics*, *386*(3-4), 157–175.

Horn, S., & Schmincke, H-U. (2000). Volatile emission during the eruption of Baitoushan Volcano (China/North Korea) ca. 969 AD. *Bulletin of the Seismological Society of America*, *61*(8), 537–555.

Hudson, T., White, R. S., Greenfield, T., Ágústsdóttir, T., Brisbourne, A., & Green, R. G. (2017). Deep crustal melt plumbing of Bardarbunga volcano, Iceland. *Geophysical Research Letters*, *44*, 8785–8794. https://doi.org/10.1002/2017GL074749

Iacovino, K., Ju-Song, K., Sisson, T., Lowenstern, J., Kuk-Hun, R., Jong-Nam, J., et al. (2016). Quantifying gas emissions from the "Millennium Eruption" of Paektu volcano, Democratic People's Republic of Korea/China. *Science Advances*, *2*(11), e1600913.

Kim, S., Tkalčić, H., & Rhie, J. (2017). Seismic constraints on magma evolution beneath Mount Baekdu (Changbai) volcano from transdimensional Bayesian inversion of ambient noise data. *Journal of Geophysical Research: Solid Earth*, *122*, 5452–5473. https://doi.org/10.1002/2017JB014105

Kyong-Song, R., Hammond, J. O. S., Chol-Nam, K., Hyok, K., Yong-Gun, Y., Gil-Jong, P., et al. (2016). Evidence for partial melt in the crust beneath Mt. Paektu (Changbaishan), Democratic People's Republic of Korea and China. *Science Advances*, *2*, e1501513.

Levin, V., & Park, J. (1998). P-SH conversions in a layered media with hexagonally symmetric anisotropy: A cookbook. *Pure and Applied Geophysics*, *151*, 669–697.

Liu, R., Fan, Q., Zheng, X., Zhang, M., & Li, N. (1998). The magma evolution of Tianchi volcano, Changbaishan. *Science in China Series D: Earth Sciences*, *41*(4), 382–389.

Liu, Z., Zhang, X.-K., Wang, F.-Y., Duan, Y.-H., & Lai, X.-l. (2005). 2-D crustal Poisson's ratio from seismic travel time inversion in Changbaishan Tianchi volcanic region. *Acta Seismologica Sinica*, *18*(3), 345–353.

Lodge, A., & Helffrich, G. (2009). Grid-search inversion of teleseismic receiver functions. *Geophysical Journal International*, *178*, 513–523.

Nanayama, F., Satake, K., Furukawa, R., Shimokawa, K., Atwater, B. F., Shigeno, K., & Yamaki, S. (2003). Unusually large earthquakes inferred from tsunami deposits along the Kuril trench. *Nature*, *424*(6949), 660–663.

Niu, F., & Li, J. (2011). Component azimuths of the CEArray stations estimated from P-wave particle motion. *Earthquake Science*, *24*(1), 3–13.

Oppenheimer, C., Wacker, L., Xu, J., Galván, J. D., Stoffel, M., Guillet, S., et al. (2017). Multi-proxy dating the Millennium Eruption of Changbaishan to late 946 CE. *Quaternary Science Reviews*, *158*, 164–171.

Paek, R. J. (1996). *Geology of Korea*. Pyongyang: Foreign Publishing House.

Pan, B., de Silva, S. L., Xu, J., Chen, Z., Miggins, D. P., & Wei, H. (2017). The VEI-7 Millennium Eruption, Changbaishan-Tianchi volcano, China/DPRK: New field, petrological, and chemical constraints on stratigraphy, volcanology, and magma dynamics. *Journal of Volcanology and Geothermal Research*, *343*, 45–59.

Piana Agostinetti, N., & Amato, A. (2009). Moho depth and *Vp/Vs* ratio in peninsular Italy from teleseismic receiver functions. *Journal of Geophysical Research*, *114*, B06303. https://doi.org/10.1029/2008JB005899

Qiu, G. G., Pei, F. G., Fang, H., Fang, H., Du, B. R., Zhang, X. B., et al. (2014). Analysis of magma chamber at the Tianchi volcano area in Changbai mountain. *Chinese Journal of Geophysics*, *57*(10), 3466–3477. (in Chinese).

Ramalho, R. S., Helffrich, G., Madeira, J., Cosca, M., Thomas, C., Quartau, R., et al. (2017). Emergence and evolution of Santa Maria Island (Azores)—The conundrum of uplifted islands revisited. *Geology*, *129*(3-4), 372–390.

Ramos, F. C., Heizler, M. T., Buettner, J. E., Gill, J. B., Wei, H. Q., Dimond, C. A., & Scott, S. R. (2016). U-series and ^{40}Ar/^{39}Ar ages of Holocene volcanic rocks at Changbaishan volcano, China. *Geology*, *44*(7), 511–514.

Ramos, F. C., Wolff, J., Buettner, J., Wei, H., & Xu, J. (2019). Ra/Th ages of sanidine in young trachytes erupted at Changbaishan Volcano, China. *Journal of Volcanology and Geothermal Research*, *374*, 226–241.

Ren, J., Niu, B., Wang, J., Jin, X., Zhao, L., & Liu, R. (2013). 1:5 million international geological map of Asia. *Journal of Asian Earth Sciences*, *72*(C), 3–11.

Savage, M. K. (1998). Lower crustal anisotropy or dipping boundaries? Effects on receiver functions and a case study in New Zealand. *Journal of Geophysical Research*, *103*, 15069–15087.

Schmandt, B., Jiang, C., & Farrell, J. (2019). Seismic perspectives from the western U.S. on magma reservoirs underlying large silicic calderas. *Journal of Volcanology and Geothermal Research*, *384*, 158–178.

Schulte-Pelkum, V., & Mahan, K. H. (2014). A method for mapping crustal deformation and anisotropy with receiver functions and first results from USArray. *Earth and Planetary Science Letters*, *402*, 221–233.

Song, J., Hetland, E. A., Wu, F. T., Zhang, X., Liu, G., & Yang, Z. (2007). *P*-wave velocity structure under the Changbaishan volcanic region, NE China, from wide-angle reflection and refraction data. *Tectonophysics*, *433*(1-4), 127–139.

Sparks, R. S. J., Annen, C. J., Blundy, J., Cashman, K., Rust, A., & Jackson, M. (2019). Formation and dynamics of magma reservoirs. *Philosophical Transactions of the Royal Society London A*, *377*, 20180019.

Stone, R. (2011). Vigil at North Korea's Mount Doom. *Science*, *334*(6056), 584–588.

Stuart, G. W., Bastow, I. D., & Ebinger, C. J. (2006). Crustal structure of the northern Main Ethiopian Rift from receiver function studies. In G. Yirgu, C. J. Ebinger, & P. K. H., Maguire (Eds.), *The Afar volcanic province within the east African rift system* (pp. 55–72). London, UK: Geological Society, Special Publication.

Sun, C., Plunkett, G., Liu, J., Zhao, H., Sigl, M., McConnell, J. R., et al. (2014). Ash from Changbaishan Millennium Eruption recorded in Greenland ice: Implications for determining the eruption's timing and impact. *Geophysical Research Letters*, *41*, 694–701. https://doi.org/10.1002/2013GL058642

Tang, J., Deng, Q., Zhao, G., Bai, D., Jin, G., Li, W., et al. (2001). Electric conductivity and magma chamber at the Tianchi Volcano area in Changbaishan Mountain. *Seismology and Geology*, *23*, 191–200.

Tang, Y., Obayashi, M., Niu, F., Grand, S. P., Chen, Y. J., Kawakatsu, H., et al. (2014). Changbaishan volcanism in northeast China linked to subduction-induced mantle upwelling. *Nature Geoscience*, *7*(6), 470–475.

The Mount Peaktu Geoscientific Group (MPGG) (2013). Mt. Paektu Seismic Network. International Federation of Digital Seismograph Networks. Other/Seismic Network.

Vanorio, T., Prasad, M., Patella, D., & Nur, A. (2002). Ultrasonic velocity measurements in volcanic rocks: Correlation with microtexture. *Geophysical Journal International*, *149*(1), 22–36.

Ward, K. M., Zandt, G., Beck, S. L., Christensen, D. H., & McFarlin, H. (2014). Seismic imaging of the magmatic underpinnings beneath the Altiplano-Puna volcanic complex from the joint inversion of surface wave dispersion and receiver functions. *Earth and Planetary Science Letters*, *404*, 43–53.

Wei, W., Hammond, J. O. S., Zhao, D., Xu, J., Liu, Q., & Gu, Y. (2019). Seismic evidence for a mantle transition zone origin of the Wudalianchi and Halaha volcanoes in Northeast China. *Geochemistry, Geophysics, Geosystems*, *20*, 398–416. https://doi.org/10.1029/2018GC007663

Wei, H., Liu, G., & Gill, J. (2013). Review of eruptive activity at Tianchi volcano, Changbaishan, northeast China: Implications for possible future eruptions. *Bulletin of Volcanology*, *75*(4), 1–14.

Wei, W., Xu, J., Zhao, D., & Shi, Y. (2012). East Asia mantle tomography: New insight into plate subduction and intraplate volcanism. *Journal of Asian Earth Sciences*, *60*, 88–103.

White, R., Smith, L., Roberts, A., Christie, P., & Kusznir, N. (2008). Lower-crustal intrusion on the North Atlantic continental margin. *Nature*, *452*(7186), 460–464.

Wu, F. (1998). Study of Changbai volcanoes and deep subduction zone. International Federation of Digital Seismograph Networks. Dataset/Seismic Network.

Wu, J., Jiao, W., Ming, Y., & Su, W. (2006). Attenuation of coda waves at the Changbaishan Tianchi volcanic area in Northeast China. *Pure and Applied Geophysics*, *163*(7), 1351–1368.

Wu, J., Ming, Y., Fang, L., & Wang, W. (2009). *S*-wave velocity structure beneath Changbaishan volcano inferred from receiver function. *Earthquake Science*, *22*, 409–416.

Wu, J., Ming, Y., Yiming, L., Shengfu, Q., & SongYong, Y. (2002). A study on the micro-earthquake swarm occurred on Aug. 20, 2002 in Changbaishan Tianchi volcano. *Seismological and Geomagnetic Observation and Research*, *4*, 1–8.

Wu, J., Ming, Y.-H., Zhang, H.-R., Liu, G.-M., Fang, L.-H., Su, W., & Wang, W.-L. (2007). Earthquake swarm activity in Changbaishan Tianchi Volcano. *Chinese Journal of Geophysics*, *50*(4), 938–946.

Xu, J., Liu, G., Wu, J., Ming, Y., Wang, Q., Cui, D., et al. (2012). Recent unrest of Changbaishan volcano, northeast China: A precursor of a future eruption? *Geophysical Research Letters*, *39*, L16305. https://doi.org/10.1029/2012GL052600

Xu, J., Pan, B., Liu, T., Hajdas, I., Zhao, B., Yu, H., et al. (2013). Climatic impact of the Millennium Eruption of Changbaishan volcano in China: New insights from high-precision radiocarbon wiggle-match dating. *Geophysical Research Letters*, *40*, 54–59. https://doi.org/10.1029/2012GL054246

Yang, Y., Lei, J., Ai, Y., Zhang, G., Sun, C., Fan, E., et al. (2019). Crustal structure beneath Northeast China from ambient noise tomography. *Physics of the Earth and Planetary Interiors*, *293*, 106257.

Zhang, X.-K., Zhang, C.-K., Zhao, J.-R., Yang, Z.-X., Li, S.-L., Zhang, J.-S., et al. (2002). Deep seismic sounding investigation into the deep structure of the magma system in Changbaishan-Tianchi volcanic region. *Acta Seismologica Sinica*, *15*(2), 143–151.

Zhao, D. (2004). Global tomographic images of mantle plumes and subducting slabs: Insight into deep Earth dynamics. *Physics of the Earth and Planetary Interiors*, *146*(1-2), 3–34.

Zhu, L., & Kanamori, H. (2000). Moho depth variation in Southern California from teleseismic receiver functions. *Journal of Geophysical Research*, *105*(B2), 2969–2980.

Zhu, H., Tian, Y., Zhao, D., Li, H., & Liu, C. (2019). Seismic structure of the Changbai intraplate volcano in NE China from joint inversion of ambient noise and receiver functions. *Journal of Geophysical Research: Solid Earth*, *124*, 4984–5002. https://doi.org/10.1029/2018JB016600